Nonlinear Dyn (2012) 67:1053–1065
DOI 10.1007/s11071-011-0048-9

ORIGINAL PAPER

An enhanced multi-term harmonic balance solution for nonlinear period-one dynamic motions in right-angle gear pairs

Junyi Yang · Tao Peng · Teik C. Lim

Received: 15 November 2010 / Accepted: 7 April 2011 / Published online: 4 May 2011

Abstract A nonlinear time-varying dynamic model for right-angle gear pair systems, considering both backlash and asymmetric mesh effects, is formulated. The mesh parameters that are characteristically time-varying and asymmetric include mesh stiffness, directional rotation radius and mesh damping. The period-one dynamic motions are obtained by solving the dimensionless equation of gear motion using an enhanced multi-term harmonic balance method (HBM) with a modified discrete Fourier Transform process and the numerical continuation method. The accuracy of the enhanced HBM solution is verified by comparison of its results to the more computational intensive, direct numerical integration calculations. Also, the Floquet theory is applied to determine the stability of the steady-state harmonic balance solutions. Finally, a set of parametric studies are performed to determine quantitatively the effects of the variation and asymmetry in mesh stiffness and directional rotation radius on the gear dynamic responses.

Keywords Right-angle gear pairs · Asymmetric mesh · Gear backlash · Nonlinear gear dynamics · Multi-term harmonic balance

J. Yang · T. Peng · T.C. Lim (✉)
Vibro-Acoustics and Sound Quality Research Laboratory, School of Dynamic Systems, Mechanical Engineering, College of Engineering and Applied Science, University of Cincinnati, 598 Rhodes Hall, P.O. Box 210072, Cincinnati, OH 45221-0072, USA
e-mail: teik.lim@uc.edu

Nomenclatures

b	gear backlash
c	mesh damping coefficient
e	static transmission error
f	nonlinear displacement
F	forcing function
h	arc-length
I_p, I_g	Pinion and gear inertias
$\vec{j}_l$	unit vector along shaft axis
J	Jacobian matrix
k	mesh stiffness function
m_e	equivalent mass function
$\vec{n}_{lm}$	line of action unit vector
$\vec{r}_{lm}$	mesh point
r	mean value ratio
s_l	pinion/gear coordinate system
t	time
T_p, T_g	load on pinion and gear
x	$\delta - e$
Δx	perturbation of x
y	perturbation state vector
δ	dynamic transmission error
λ	directional rotation radius
ω	frequency
ς	damping ratio
θ	rotational displacement

Subscripts

c	coast side
d	drive side
da	damping

k	label for stiffness
l	pinion ($l = p$) and gear ($l = g$)
m	drive ($m = d$) and coast ($m = c$) sides
n	natural mode
1	mean value
2, 3, ...	alternative value

Superscripts

$\bullet$	derivative w.r.t. time
$'$	derivative w.r.t. dimensionless time
$\rightarrow$	vector quantities
$\sim$	dimensionless quantities

1 Introduction

In the past two decades, the nonlinear frequency response spectra of parallel axis gears have been extensively studied. In those studies [1–12], particular attention was given to the formulation of the nonlinear gear dynamic models and the development of analytical, semi-analytical and numerical solution methods. Using different mesh stiffness models, including piecewise linear time-invariant (PLTI) [1, 2], piecewise linear time-varying (PLTV) [3–6] and piecewise nonlinear time-varying (PNTV) [7, 8] ones, various nonlinear representations of the parallel axis gear pair were constructed and the corresponding one degree-of-freedom (DOF) dimensionless equation of motions were formulated. The method was also extended to develop the multiple DOFs nonlinear models of multi-mesh gear trains [9, 10], geared rotor-bearing systems [11] and planetary gear sets [12]. Using various solution techniques, including analog simulation [1], digital simulation [1, 2], numerical integration [6–10], harmonic balance method (HBM) [1, 2], multi-scale method [3, 6] and multi-term HBM [4, 5, 7–12], the dimensionless equations of motion were solved for the gear dynamic response. Amongst the various solutions analyzed, the multi-term HBM coupled with the discrete Fourier Transform was shown to be capable of studying a wide range of nonlinear dynamic models of parallel axis gears [7–12], and the effectiveness was demonstrated by comparison to experimental results [4, 5] as well as direct numerical integration calculations [7–12]. Also, the computational cost of the multi-term HBM is much lower as compared to other solution schemes, and it appears that all the harmonic solutions, including stable and unstable dynamics, can be predicted. Research studies on geared rotor dynamics have also been performed extensively in Europe, for example, by Velex and his colleagues [13, 14] in France. The history of the mathematical models used in gear dynamics up until 1987 are well documented in the review paper [15] that presented five overlapping categories used to classify the nature of models proposed.

In spite of the vast number of studies directed at parallel axis gears, relatively few open publications on the topic of nonlinear dynamics of right-angle gears such as hypoid and spiral bevel types can be found. This is in part due to the complex mesh mechanism in this class of gears. Unlike the spur gear, the lines of action in these right-angle gears are not constant during the meshing process. This complexity is mainly due to the curvature feature of the hypoid gear tooth geometry and kinematics. For the same reason, the mesh coupling between the pinion and gear are not symmetric unlike parallel axis gears. In earlier studies, dynamic studies of right angle gears are limited to system level trial-and-error testing and relatively simple mathematical models. A vibration model having two degrees of freedom for a bevel gear pair was adopted [16], in which the line-of-action vector was simulated by a sine curve. In [17], it was shown experimentally that axle gear noise can be reduced in some cases by modifying the vibration mode with an inertia disk mounted on the final drive. Most recently, in a set of studies by Cheng and Lim [18–22], an analytical modeling framework for analyzing the vibration characteristics of hypoid and bevel geared rotor systems was developed. Using that framework, a nonlinear model with PLTV mesh stiffness, time-varying (TV) directional rotation radius and backlash nonlinearity was formulated and solved using the direct numerical integration [22–25]. Also, a nonlinear model considering PLTV mesh stiffness and backlash nonlinearity was proposed and analyzed using HBM by Jiang [23]. Although the effect of tooth mesh stiffness asymmetric nonlinearity on the dynamic response was analyzed using direct numerical integration [26], there is no known study that has addressed the directional rotation radius asymmetric nonlinearity, which is one of the motivations of the present analysis.

In this study, considering both backlash and asymmetric mesh nonlinearity, a complete nonlinear dynamic model for right-angle gear pairs is proposed. In the proposed formulation, the mesh stiffness, di-

rectional rotation radius and mesh damping are assumed to be time-varying and asymmetric. The multi-term HBM coupled with a modified discrete Fourier Transform (DFT) process and the numerical continuation method [27, 28] are applied to solve the dimensionless equation of motion for the gear dynamic displacement response. The symmetric or asymmetric nonlinear restoring force, damping force and external excitation forces are first calculated at each time point within one mesh period. Second, the DFT process is performed to obtain the coefficients of the fundamental frequency and its harmonics. Third, the dynamic response is derived from the solution of the harmonic balance equations. The results of the proposed enhanced multi-term HBM is validated by comparison to the more computationally intensive, direct numerical integration calculations. Finally, the effects of key parameters including the variation and asymmetry in the mesh stiffness and directional rotation radius on the gear dynamic responses is studied systematically through a series of parametric studies.

2 Mathematical model

The two degree-of-freedom torsional vibration model and the coordinate systems of a right-angle gear pair are shown in Fig. 1. The shaft and bearing are considered as rigid, and pinion and gear are modeled as rigid bodies. The mesh coupling between the pinion and gear is represented using a set of mesh stiffness and damping elements acting along a line of action dictated by the directional rotation radius. These mesh parameters are all considered as time-varying and asymmetric. The equation of motion can be derived as

$$I_p\ddot{\theta}_p + \lambda_p(\delta)c(\delta)\left(\dot{\delta} - \dot{e}\right) + \lambda_p(\delta)k(\delta)f(\delta - e) = T_p, \tag{1a}$$

$$I_g\ddot{\theta}_g - \lambda_g(\delta)c(\delta)\left(\dot{\delta} - \dot{e}\right) - \lambda_g(\delta)k(\delta)f(\delta - e) = -T_g, \tag{1b}$$

where I_p and I_g are the mass moments of inertial of pinion and gear, T_p and T_g are the torque applied on pinion and gear, and $c(\delta)$ and $k(\delta)$ are the asymmetric time-varying mesh damping and stiffness coefficients given by

$$c(\delta) = \begin{cases} c_d, & \delta \geq 0, \\ c_c, & \delta < 0, \end{cases} \tag{2}$$

$$k(\delta) = \begin{cases} k_d, & \delta \geq 0, \\ k_c, & \delta < 0, \end{cases} \tag{3}$$

$$k_d = k_{d1} + \sum_{a=1}^{A}\left(k_{d(2a)}\cos(a\omega t) + k_{d(2a+1)}\sin(a\omega t)\right), \tag{4}$$

$$k_c = k_{c1} + \sum_{b=1}^{B}\left(k_{c(2b)}\cos(b\omega t) + k_{c(2b+1)}\sin(b\omega t)\right), \tag{5}$$

$$c_d = c_{d1} + \sum_{h=1}^{H}\left(c_{d(2h)}\cos(h\omega t) + c_{d(2h+1)}\sin(h\omega t)\right), \tag{6}$$

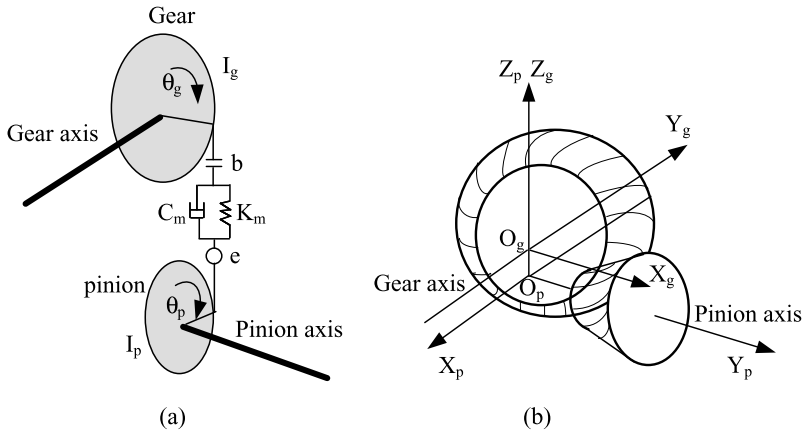

Fig. 1 (**a**) Two degrees of freedom torsional vibration model of a hypoid gear pair. (**b**) Pinion and gear coordinate systems

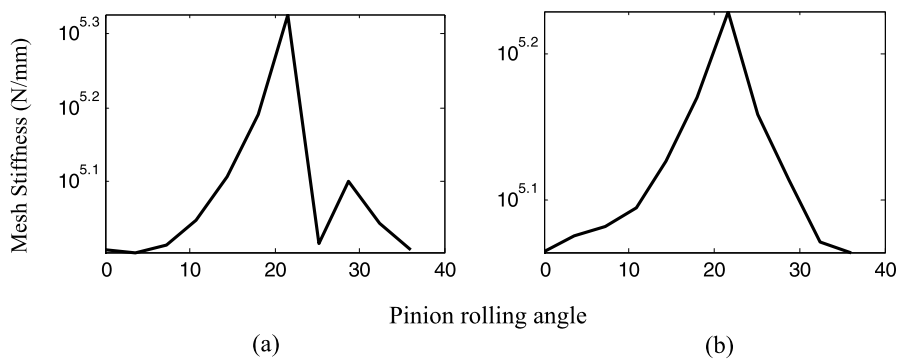

Fig. 2 Asymmetric nature of hypoid gear mesh stiffness: (**a**) drive side, (**b**) coast side

$$c_c = c_{c1} + \sum_{j=1}^{J}\big(c_{c(2j)}\cos(j\omega t) + c_{c(2j+1)}\sin(j\omega t)\big), \tag{7}$$

where c_m and k_m ($m = d, c$ for drive and coast side, respectively) are the mesh damping and stiffness for different tooth sides in contact. Typical drive and coast side mesh stiffness, obtained by synthesizing from the loaded tooth contact analysis results [22], are shown in Fig. 2. The plot clearly illustrates the asymmetric nature of the mesh stiffness for the drive and coast side cases. Similarly, other mesh parameters such as mesh damping, mesh points and line-of-action are all asymmetric. For brevity, they are not plotted here. Also, in (1), $\lambda_p(\delta)$ and $\lambda_g(\delta)$ are the asymmetric time-varying directional rotation radii of the pinion and gear. They can be expressed as

$$\lambda_p(\delta) = \begin{cases} \lambda_{pd}, & \delta \geq 0, \\ \lambda_{pc}, & \delta < 0, \end{cases} \tag{8}$$

$$\lambda_g(\delta) = \begin{cases} \lambda_{gd}, & \delta \geq 0, \\ \lambda_{gc}, & \delta < 0, \end{cases} \tag{9}$$

$$\lambda_{pd} = \lambda_{pd1} + \sum_{l=1}^{L}\big(\lambda_{pd(2l)}\cos(l\omega t) + \lambda_{pd(2l+1)}\sin(l\omega t)\big), \tag{10}$$

$$\lambda_{pc} = \lambda_{pc1} + \sum_{m=1}^{M}\big(\lambda_{pc(2m)}\cos(m\omega t) + \lambda_{pc(2m+1)}\sin(m\omega t)\big), \tag{11}$$

$$\lambda_{gd} = \lambda_{gd1} + \sum_{u=1}^{U}\big(\lambda_{gd(2u)}\cos(u\omega t) + \lambda_{gd(2u+1)}\sin(u\omega t)\big), \tag{12}$$

$$\lambda_{gc} = \lambda_{gc1} + \sum_{v=1}^{V}\big(\lambda_{gc(2v)}\cos(v\omega t) + \lambda_{gc(2v+1)}\sin(v\omega t)\big), \tag{13}$$

where λ_{pm} and λ_{gm} are the pinion and gear directional rotation radii for drive ($m = d$) and coast ($m = c$) sides of the teeth in contact. The directional rotation radii are explicitly defined as

$$\lambda_{lm} = \vec{n}_{lm} \cdot \big(\vec{j}_l \times \vec{r}_{lm}\big), \tag{14}$$

where $\vec{n}_{lm}$ and $\vec{r}_{lm}$ are the line of action and mesh point, respectively, in the coordinate system s_l for different tooth sides in contact ($l = p, q$ for pinion and gear, $m = d, c$ for drive side and coast side), and $\vec{j}_l$ is the unit vector along the pinion or gear rotating axis in the coordinate system s_l ($l = p, q$ for pinion and gear). Additionally, in (1), the nonlinear displacement function $f(\delta - e)$ is given by

$$f(\delta - e) = \begin{cases} \delta - e - b, & \delta - e \geq b, \\ 0, & -b < \delta - e < b, \\ \delta - e + b, & \delta - e \leq -b, \end{cases} \tag{15}$$

where $2b$ is the total gear backlash.

The mesh stiffness, mesh damping, directional rotation radii, and nonlinear displacement are all a function of the dynamic transmission error δ that is defined as

$$\delta = \lambda_p(\delta)\theta_p - \lambda_g(\delta)\theta_g. \tag{16}$$

The kinematic transmission error e under no or very light load is the source of internal excitation in the system. Its harmonic expression can be shown to be

$$e = \sum_{y=1}^{Y}\big(e_{(2y)}\cos(y\omega t) + e_{(2y+1)}\sin(y\omega t)\big). \tag{17}$$

The mean value of the kinematic transmission error is set to zero since it will not affect the dynamic responses. This can be seen clearly from (18a) in which only the second order derivative of the kinematic transmission error with respect to time is present as part of the excitation term on the right hand side of the equation.

The above two degrees-of-freedom, semi-definite vibration system expressed by (1) can be simplified into a single degree-of-freedom, definite vibration model since there is no constraint on the rotational coordinates of both the pinion and gear. Let $x = \delta - e$, (1a)–(1b) can be combined into the following single equation of motion:

$$m_e(\delta)\ddot{x} + c(\delta)\dot{x} + k(\delta) f(x) = m_e(\delta)\left(\frac{\lambda_p(\delta)T_p}{I_p} + \frac{\lambda_g(\delta)T_p}{I_p} - \ddot{e}\right), \tag{18a}$$

$$m_e(\delta) = \begin{cases} m_{ed}, & \delta \geq 0, \\ m_{ec}, & \delta < 0, \end{cases} \tag{18b}$$

$$m_{ed} = 1/\left(\lambda_{pd}^2/I_p + \lambda_{gd}^2/I_g\right), \tag{18c}$$

$$m_{ec} = 1/\left(\lambda_{pc}^2/I_p + \lambda_{gc}^2/I_g\right), \tag{18d}$$

$$f(x) = \begin{cases} x - b, & x \geq b, \\ 0, & -b < x < b, \\ x + b, & x \leq b. \end{cases} \tag{18e}$$

Also, during the simplification process, $\dot{\lambda}_{lm}$ and $\ddot{\lambda}_{lm}$ are assumed to be zero. It is a reasonable assumption since the mesh point and line of action are typically continuous without abrupt change even though they are inherently time-varying.

For simplicity, consider $m_{ed1} = 1/(\lambda_{pd1}^2/I_p + \lambda_{gd1}^2/I_g)$, and $\omega_n = \sqrt{k_{d1}/m_{ed1}}$. Then, to derive the dimensionless equation of motion, the following transformations are applied:

$$\tilde{x} = x/b, \tag{19}$$

$$\tilde{t} = \omega_n t, \tag{20}$$

$$\tilde{\omega} = \omega/\omega_n, \tag{21}$$

$$\tilde{k}_d = k_d/k_{d1} = 1 + \sum_{a=1}^{A}\left(\tilde{k}_{d(2a)}\cos\left(a\tilde{\omega}\tilde{t}\right) + \tilde{k}_{d(2a+1)}\sin\left(a\tilde{\omega}\tilde{t}\right)\right), \tag{22}$$

$$\tilde{k}_c = k_c/k_{c1} = 1 + \sum_{b=1}^{B}\left(\tilde{k}_{c(2b)}\cos\left(b\tilde{\omega}\tilde{t}\right) + \tilde{k}_{c(2b+1)}\sin\left(b\tilde{\omega}\tilde{t}\right)\right), \tag{23}$$

$$\tilde{c}_d = c_d/c_{d1} = 1 + \sum_{h=1}^{H}\left(\tilde{c}_{d(2h)}\cos\left(h\tilde{\omega}\tilde{t}\right) + \tilde{c}_{d(2h+1)}\sin\left(h\tilde{\omega}\tilde{t}\right)\right), \tag{24}$$

$$\tilde{c}_c = c_c/c_{c1} = 1 + \sum_{j=1}^{J}\left(\tilde{c}_{c(2j)}\cos\left(j\tilde{\omega}\tilde{t}\right) + \tilde{c}_{c(2j+1)}\sin\left(j\tilde{\omega}\tilde{t}\right)\right), \tag{25}$$

$$\tilde{\lambda}_{pd} = \lambda_{pd}/\lambda_{pd1} = 1 + \sum_{l=1}^{L}\left(\tilde{\lambda}_{pd(2l)}\cos\left(l\tilde{\omega}\tilde{t}\right) + \tilde{\lambda}_{pd(2l+1)}\sin\left(l\tilde{\omega}\tilde{t}\right)\right), \tag{26}$$

$$\tilde{\lambda}_{pc} = \lambda_{pc}/\lambda_{pc1} = 1 + \sum_{m=1}^{M}\left(\tilde{\lambda}_{pc(2m)}\cos\left(m\tilde{\omega}\tilde{t}\right) + \tilde{\lambda}_{pc(2m+1)}\sin\left(m\tilde{\omega}\tilde{t}\right)\right), \tag{27}$$

$$\tilde{\lambda}_{gd} = \lambda_{gd}/\lambda_{gd1} = 1 + \sum_{u=1}^{U}\left(\tilde{\lambda}_{gd(2u)}\cos\left(u\tilde{\omega}\tilde{t}\right) + \tilde{\lambda}_{gd(2u+1)}\sin(u\tilde{\omega}\tilde{t})\right), \tag{28}$$

$$\tilde{\lambda}_{gc} = \lambda_{gc}/\lambda_{gc1} = 1 + \sum_{v=1}^{V}\left(\tilde{\lambda}_{gc(2v)}\cos\left(v\tilde{\omega}\tilde{t}\right) + \tilde{\lambda}_{gc(2v+1)}\sin(v\tilde{\omega}\tilde{t})\right), \tag{29}$$

$$\tilde{e} = e/b = \sum_{y=1}^{Y}\left(\tilde{e}_{(2y)}\cos\left(y\tilde{\omega}\tilde{t}\right) + \tilde{e}_{(2y+1)}/b\sin(y\tilde{\omega}\tilde{t})\right). \tag{30}$$

Accordingly, the simplified dimensionless equation of motion can be represented as

$$\tilde{x}'' + 2\zeta c\left(\tilde{x}\right)g\left(\tilde{x}\right)\tilde{x}' + \frac{g(\tilde{x})}{1+\sigma}k\left(\tilde{x}\right)f\left(\tilde{x}\right) = \tilde{T}_p\tilde{\lambda}_p\left(\tilde{x}\right) + \tilde{T}_g\tilde{\lambda}_g\left(\tilde{x}\right) - \tilde{e}'', \tag{31a}$$

where the symbols in the above equation are given by

$$\zeta = \frac{\lambda_{pd1}^2 c_{d1}}{2I_p\omega_n}, \tag{31b}$$

$$\sigma = \frac{\lambda_{gd1}^2 I_p}{\lambda_{pd1}^2 I_g}, \tag{31c}$$

$$\tilde{T}_p = \frac{\lambda_{pd1} T_p}{b\omega_n I_p}, \tag{31d}$$

$$\tilde{T}_g = \sigma \tilde{T}_p, \tag{31e}$$

$$c(\tilde{x}) = \begin{cases} \tilde{c}_d, & \tilde{x} \geq 1, \\ r_{da}\tilde{c}_c, & \tilde{x} < 1, \end{cases} \tag{31f}$$

$$r_{da} = \frac{c_{c1}}{c_{d1}}, \tag{31g}$$

$$k(\tilde{x}) = \begin{cases} \tilde{k}_d, & \tilde{x} \geq 1, \\ r_k\tilde{k}_c, & \tilde{x} < 1, \end{cases} \tag{31h}$$

$$r_k = \frac{k_{c1}}{k_{d1}}, \tag{31i}$$

$$f(\tilde{x}) = \begin{cases} \tilde{x} - 1, & \tilde{x} \geq 1, \\ 0, & -1 < \tilde{x} < 1, \\ \tilde{x} + 1 & \tilde{x} \leq -1, \end{cases} \tag{31j}$$

$$g(\tilde{x}) = \begin{cases} \tilde{\lambda}_{pd}^2 + \sigma\tilde{\lambda}_{gd}^2, & \tilde{x} \geq 0, \\ r_p^2\tilde{\lambda}_{pc}^2 + \sigma r_g^2\tilde{\lambda}_{gc}^2, & \tilde{x} < 0, \end{cases} \tag{31k}$$

$$\tilde{\lambda}_p(\tilde{x}) = \begin{cases} \tilde{\lambda}_{pd}, & \tilde{x} \geq 1, \\ r_p\tilde{\lambda}_{pc}, & \tilde{x} < 1, \end{cases} \tag{31l}$$

$$\tilde{\lambda}_g(\tilde{x}) = \begin{cases} \tilde{\lambda}_{gd}, & \tilde{x} \geq 1, \\ r_g\tilde{\lambda}_{gc}, & \tilde{x} < 1, \end{cases} \tag{31m}$$

$$r_p = \frac{\lambda_{pc1}}{\lambda_{pd1}}, \tag{31n}$$

$$r_g = \frac{\lambda_{gc1}}{\lambda_{gd1}}. \tag{31o}$$

Next, the period-one solution of (31a) is discussed.

3 Period-one dynamics

The multi-term harmonic balance method coupled with DFT, which has been successfully applied in [4, 5, 7–12] to analyze spur gear nonlinear dynamics, is adopted in this study to solve the dimensionless equation of motion for $\tilde{x}$. In those previous studies, the DFT was applied to calculate the Fourier coefficients of the nonlinear displacement. Here in this analysis, the DFT is extended to calculate the Fourier coefficients of the damping, nonlinear restoring and external excitation forces.

To start the derivation, the steady-state solution is assumed to be of the form

$$\tilde{x}(t) = \tilde{x}_1 + \sum_{r=1}^{R}\left(\tilde{x}_{2r}\cos\left(r\tilde{\omega}\tilde{t}\right) + \tilde{x}_{2r+1}\sin\left(r\tilde{\omega}\tilde{t}\right)\right), \tag{32}$$

which can be differentiated to yield

$$\tilde{x}'(t) = \sum_{r=1}^{R}\left(-r\tilde{\omega}\tilde{x}_{2r}\sin\left(r\tilde{\omega}\tilde{t}\right) + r\tilde{\omega}\tilde{x}_{2r+1}\cos\left(r\tilde{\omega}\tilde{t}\right)\right). \tag{33}$$

Then, the time series of the damping, nonlinear restoring and external excitation forces can be obtained by sampling even number of n points within one fundamental mesh period. Here, n must be larger than $2R$ where R is the highest harmonics of the solution of interest. Using this process, the time series of the damping force can be shown to be:

$$F_{da}(\tilde{t}_i) = 2\zeta c\left(\tilde{x}(\tilde{t}_i)\right)g\left(\tilde{x}(\tilde{t}_i)\right)\tilde{x}'(\tilde{t}_i), \quad i = 0, 1, 2, \ldots, n-1. \tag{34}$$

Similarly, the time series of the nonlinear restoring force is

$$F_k(\tilde{t}_i) = \frac{g(\tilde{x}(\tilde{t}_i))}{1+\sigma}k\left(\tilde{x}(\tilde{t}_i)\right)f\left(\tilde{x}(\tilde{t}_i)\right), \quad i = 0, 1, 2, \ldots, n-1; \tag{35}$$

and the time series of the external excitation forces are

$$F_p(\tilde{t}_i) = \tilde{T}_p\tilde{\lambda}_p\left(\tilde{x}(\tilde{t}_i)\right), \quad i = 0, 1, 2, \ldots, n-1; \tag{36}$$

$$F_g(\tilde{t}_i) = \tilde{T}_g\tilde{\lambda}_g\left(\tilde{x}(\tilde{t}_i)\right), \quad i = 0, 1, 2, \ldots, n-1. \tag{37}$$

In order to use the multi-term HBM, all of these force terms must be represented by Fourier series as follows:

$$F_{da} = F_{da1} + \sum_{r=1}^{R} F_{da(2r)}\cos\left(r\tilde{\omega}\tilde{t}\right) + F_{da(2r+1)}\sin\left(r\tilde{\omega}\tilde{t}\right), \tag{38}$$

$$F_k = F_{k1} + \sum_{r=1}^{R} F_{k(2r)}\cos\left(r\tilde{\omega}\tilde{t}\right) + F_{k(2r+1)}\sin\left(r\tilde{\omega}\tilde{t}\right), \tag{39}$$

$$F_p = F_{p1} + \sum_{r=1}^{R} F_{p(2r)} \cos\left(r\tilde{\omega}\tilde{t}\right) + F_{p(2r+1)} \sin\left(r\tilde{\omega}\tilde{t}\right), \tag{40}$$

$$F_q = F_{q1} + \sum_{r=1}^{R} F_{q(2r)} \cos\left(r\tilde{\omega}\tilde{t}\right) + F_{q(2r+1)} \sin\left(r\tilde{\omega}\tilde{t}\right), \tag{41}$$

where the coefficients of each series can be calculated using the discrete Fourier Transform. They are explicitly given by

$$F_{da1} = \frac{1}{n}\sum_{i=0}^{n-1} F_{da}(t_i), \tag{42a}$$

$$F_{da(2r)} = \frac{2}{n}\sum_{i=0}^{n-1} F_{da}(t_i)\cos(2\pi r t_i), \tag{42b}$$

$$F_{da(2r+1)} = \frac{2}{n}\sum_{i=0}^{n-1} F_{da}(t_i)\sin(2\pi r t_i), \quad r = 0, 1, 2, \ldots, R, \tag{42c}$$

$$F_{k1} = \frac{1}{n}\sum_{i=0}^{n-1} F_{k}(t_i), \tag{43a}$$

$$F_{k(2r)} = \frac{2}{n}\sum_{i=0}^{n-1} F_{k}(t_i)\cos(2\pi r t_i), \tag{43b}$$

$$F_{k(2r+1)} = \frac{2}{n}\sum_{i=0}^{n-1} F_{k}(t_i)\sin(2\pi r t_i), \quad r = 0, 1, 2, \ldots, R, \tag{43c}$$

$$F_{p1} = \frac{1}{n}\sum_{i=0}^{n-1} F_{p}(t_i), \tag{44a}$$

$$F_{p(2r)} = \frac{2}{n}\sum_{i=0}^{n-1} F_{p}(t_i)\cos(2\pi r t_i), \tag{44b}$$

$$F_{p(2r+1)} = \frac{2}{n}\sum_{i=0}^{n-1} F_{p}(t_i)\sin(2\pi r t_i), \quad r = 0, 1, 2, \ldots, R, \tag{44c}$$

$$F_{g1} = \frac{1}{n}\sum_{i=0}^{n-1} F_{g}(t_i), \tag{45a}$$

$$F_{g(2r)} = \frac{2}{n}\sum_{i=0}^{n-1} F_{g}(t_i)\cos(2\pi r t_i), \tag{45b}$$

$$F_{g(2r+1)} = \frac{2}{n}\sum_{i=0}^{n-1} F_{g}(t_i)\sin(2\pi r t_i), \quad r = 0, 1, 2, \ldots, R. \tag{45c}$$

Next, the algebraic sums of the coefficients of the terms of the like frequencies are forced to be equal. Doing so will yield

$$S_1 = F_{da1} + F_{k1} - F_{p1} + F_{q1}, \tag{46a}$$

$$S_{2r} = -\left(r\tilde{\omega}\right)^2 \tilde{x}_{2r} + F_{da(2r)} + F_{k(2r)} - F_{p(2r)} - F_{q(2r)} + \left(r\tilde{\omega}\right)^2 \tilde{e}_{2r}, \tag{46b}$$

$$S_{2r+1} = -\left(r\tilde{\omega}\right)^2 \tilde{x}_{2r+1} + F_{da(2r+1)} + F_{k(2r+1)} - F_{p(2r+1)} - F_{q(2r+1)} + \left(r\tilde{\omega}\right)^2 \tilde{e}_{2r+1}. \tag{46c}$$

Finally, the Newton–Raphson method is applied to solve the vector equations $S = 0$ for the solution vector $\tilde{x} = [\tilde{x}_1\ \tilde{x}_2\ \cdots\ \tilde{x}_{2R+1}]^T$. The problem statement can be expressed as follows:

$$\tilde{x}^{(m+1)} = \tilde{x}^{(m)} - \left[J^{-1}\right]^{(m)} S^{(m)}, \tag{47}$$

where the $(m+1)$th iteration of solution vector $\tilde{x}^{(m+1)}$ is calculated using the previous iteration values of $\tilde{x}^{(m)}$, $S^{(m)}$ and the Jacobian matrix $J^{(m)}$. The process is repeated until the steady-state solution $\tilde{x} = [\tilde{x}_1\ \tilde{x}_2\ \cdots\ \tilde{x}_{2R+1}]^T$ converges to within a predefined error limit for that excitation frequency. If the response at the next frequency point is needed, a control parameter is then set to the next value to restart the iteration process again. Also, it may be noted that corresponding to one excitation frequency, multiple solutions may exist for the nonlinear gear dynamic system. If the frequency is chosen as the control parameter, which is normally done, the calculations may only yield parts of the whole solution set unless one properly switches the frequency sweep directions as also seen in the earlier spur gear dynamic analysis [4, 5, 7, 8]. Fortunately, there are other choices for control parameter such as the components of the solution vector [9, 10] and the arc-length [27]. In this study, the arc-length is used as the control parameter since it is believed to be more effective and easy to formulate. The arc-length and tangential vector of the solution curve are used to predict

the initial value of the next solution point given by

$$\tilde{x}_{n+1} = \tilde{x}_n - T_n h, \tag{48}$$

where $\tilde{x}_{n+1}$ represents initial value for the $(n+1)$th point iteration, $\tilde{x}_n$ represents the solution of the nth point, T_n is the tangential vector corresponding to the solution at the nth point, and h is the arc-length increment.

The Floquet theory [29] is applied to perform the stability analysis of the steady-state solution obtained above. Consider the perturbation equation,

$$\Delta\tilde{x}'' + 2\zeta c\big(\tilde{x}(\tilde{t})\big) g\big(\tilde{x}(\tilde{t})\big)\Delta\tilde{x}' + \frac{g(\tilde{x}(\tilde{t}))}{1+\sigma}\tilde{k}\big(\tilde{x}(\tilde{t})\big) f\big(\tilde{x}(\tilde{t})\big)\Delta\tilde{x} = 0, \tag{49}$$

where $\Delta\tilde{x}$ is the small perturbation of the periodic solution $\tilde{x}(t) = \tilde{x}(t+T)$. By defining $y = [\Delta\tilde{x}\ \ \Delta\tilde{x}']^T$, the perturbation equation can be rewritten as

$$y'(\tilde{t}) = H(\tilde{t})\, y(\tilde{t}), \tag{50a}$$

$$H(\tilde{t}) = \begin{bmatrix} 0 & 1 \\ -\frac{g(\tilde{x}(\tilde{t}))}{1+\sigma}\tilde{k}(\tilde{x}(\tilde{t}))\, f(\tilde{x}(\tilde{t})) & -2\zeta c(\tilde{x}(\tilde{t}))\, g(\tilde{x}(\tilde{t})) \end{bmatrix}. \tag{50b}$$

The above differential equation is then solved for $y'(T)$ assuming the initial condition $y(0) = I_2$ where I_2 is the square identity matrix of dimension two. Then, the local stability of the steady-state solutions can be determined by analyzing the eigenvalues of $y'(T)$. The solution is considered stable when the modulus of the eigenvalues is less than unity; otherwise the solution is unstable.

4 Parametric studies

The light load case studied in [25] is taken as the baseline set, and only the period-one motions are of interest. The dimensionless right-angle hypoid gear parameters for the numerical calculations are listed in Table 1. To simplify the parametric analysis, only the first harmonic of the mesh stiffness, directional rotation radii and transmission error are considered. Also, the torque transmitted through the hypoid gear pair and the mesh damping coefficients are taken as constants.

Table 1 Dimensionless dynamic parameters for a typical automotive hypoid gear pair

Parameter symbols	Numerical value
$\tilde{T}_p$	0.1
ς	0.03
σ	0.75
$\tilde{c}_d, \tilde{c}_c$	1
$\tilde{k}_{d2}, \tilde{k}_{c2}$	−0.0405
$\tilde{k}_{d3}, \tilde{k}_{c3}$	0.0294
r_p, r_q, r_k, r_{da}	1
$\tilde{\lambda}_{pd2}, \tilde{\lambda}_{pc2}, \tilde{\lambda}_{gd2}, \tilde{\lambda}_{gc2}$	0.01
$\tilde{\lambda}_{pd3}, \tilde{\lambda}_{pc3}, \tilde{\lambda}_{gd3}, \tilde{\lambda}_{gc3}$	0
$\tilde{e}_2$	0
$\tilde{e}_3$	−0.5

First, the predictions of the multi-term HBM method are compared to the results of the less efficient, direct numerical integration. Then, the results of the parametric studies are examined to understand the effects of key parameters on the gear dynamic response.

4.1 Numerical validation

For verification purpose, the nonlinear dynamic response of the baseline right-angle hypoid gear case is obtained using both the multi-term HBM and the Runge–Kutta integration routine with variable step [25]. Their predicted dynamic responses are compared in Fig. 3, and can be seen to match with each other very well. Here, Fig. 3(a) shows the comparison of the root mean square (RMS) values of the displacement response, while the corresponding mean values are plotted in Fig. 3(b). The dimensionless results can be easily transformed back to the physical coordinate. For example, for a practical application, whose physical parameters are listed on Table 2, the dimensionless parameters are calculated as $I_p = 0.03$ kg m^2, $I_g = 0.08$ kg m^2, $\lambda_{pd1} = 0.026$ m, $\lambda_{gd1} = 0.1119$ m, as well as $k_{d1} = 1.2 \times 10^8$ N/m, and the backlash is assumed to be $b = 20$ µm, then the natural angular frequency can be obtained as $\omega_n \approx 4893$ rad/s. Thus, in Fig. 3(a), the physical frequency range is from about 154 to 1947 Hz, and the displacement range is from 0.2 to 200 µm.

The right-angle gear example selected for the numerical analysis is a hypoid type, as noted earlier.

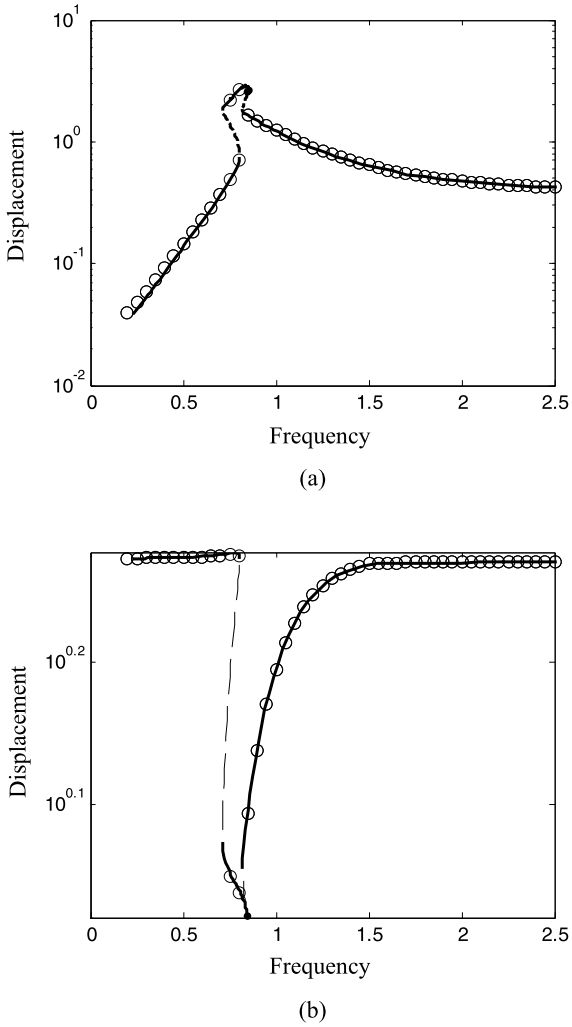

Fig. 3 Comparison of multi-term HBM and numerical integration: (**a**) RMS of the dynamic displacement, (**b**) mean value of the dynamic displacement. ——— Stable steady-state solution by multi-term HBM; – – – · Unstable steady-state solution by multi-term HBM; ○ Solutions by numerical integration

Table 2 Physical parameters of a real application hypoid gear pair

Parameter symbols	Numerical value
Pinion/gear tooth number	10/43
Pinion/gear pitch radius	0.048/0.1681 (m)
Offset	0.03175 (m)
Input torque	0.5 (N m)

From past studies [23, 25, 26], it is known that hypoid gears can manifest both single-sided and double-sided tooth impacts. This behavior is also seen here in the simulation results of both multi-term HBM and numerical integration. A closer examination of Fig. 3(a) reveals that, in the low frequency range, the hypoid gear pair behaves quite linearly with no evidence of tooth impact response. As the dimensionless frequency increases to $\tilde{\omega} = 0.8064$, the single-sided tooth impact begins to emerge. At that point, the dynamic displacement response curve veers left towards the lower frequency range unlike a typical linear system that would continue to climb in both response and frequency. This type of characteristic indicates the effect of backlash nonlinearity causing single-sided tooth impact, which is similar to a softening spring case. The response curve continues along that same trajectory as the dimensionless frequency decreases to $\tilde{\omega} = 0.7116$ from $\tilde{\omega} = 0.8064$ until double-sided tooth impact begins to show up. At this point, the effect of backlash nonlinearity manifests itself as a hardening spring case because of the additional impact with the preceding tooth. When this happens, the trajectory of the response takes a sharp turn towards the right with increasing frequency again. The dynamic displacement response reaches the peak amplitude at $\tilde{\omega} = 0.8439$. After that point, the hypoid gear pair response changes back to only single-sided tooth impact and subsequently becoming linear again as the frequency increases further.

4.2 Numerical analysis

In this section, a series of numerical simulations are performed. The purpose is to examine the effects of the magnitude variation and asymmetric nonlinearity of the mesh stiffness and directional rotation radii on the dynamic displacement response.

4.2.1 Effect of directional rotation radii variation

In this analysis, only the effect of the directional rotation radii variation is analyzed. No asymmetry is included by setting $r_p = r_q = 1$. The variation is represented by five different values of the second Fourier coefficient given by $\tilde{\lambda}_{pd2} = \tilde{\lambda}_{pc2} = \tilde{\lambda}_{gd2} = \tilde{\lambda}_{gc2} = 0.01, 0.1, 0.15, 0.18, 0.25$, which are related to the coefficients of the first order harmonic of the directional rotation radii.

The numerical results presented in Fig. 4(a) show that the increase in second Fourier coefficient or first order harmonic of the directional rotation radii

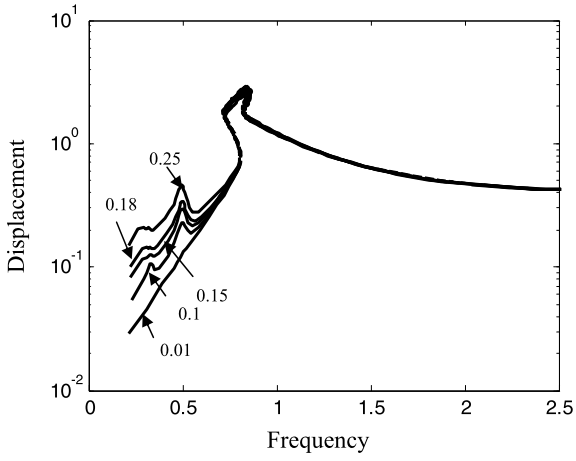

(a)

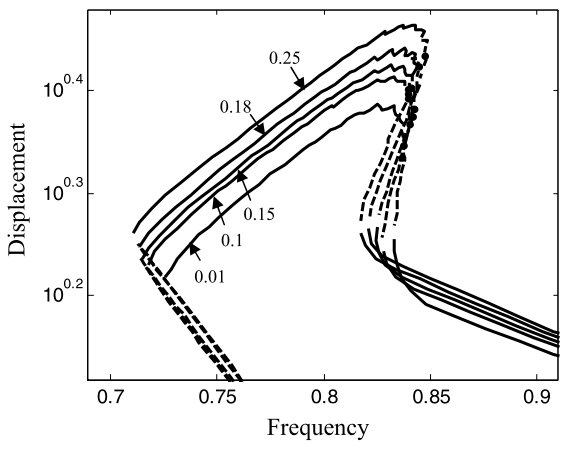

(b)

Fig. 4 Effect of the directional rotation radii variation on the dynamic response: (**a**) RMS of the dynamic displacement, (**b**) primary resonance of the dynamic displacement. ——— Stable steady-state solution by multi-term HBM; – – – · Unstable steady-state solution by multi-term HBM

seems to amplify the peak values of the second and third super-harmonic responses. When $\tilde{\lambda}_{pd2} = \tilde{\lambda}_{pc2} = \tilde{\lambda}_{gd2} = \tilde{\lambda}_{gc2} = 0.01$, no obvious peak around $\tilde{\omega} = 0.5$ and $\tilde{\omega} = 0.33$ can be found. As the second Fourier coefficient increases to 0.1, the second and third super-harmonic peaks begin to appear. The peak values of the second and third super-harmonics continue to amplify as the second Fourier coefficient are further increased.

Similar effect of the directional rotation radii variation on the primary resonance can be observed as shown in the enlarged plot around the primary resonance in Fig. 4(b). As the second Fourier coefficient of the directional rotation radii for both pinion and gear are increased, the peak value and the corresponding resonance frequency of the primary resonance seems to rise appreciably.

4.2.2 Effect of directional rotation radii asymmetric nonlinearity

To examine the effect of asymmetry in the directional rotation radii on the dynamic displacement responses, five different coast to drive sides mean value ratios given by $r_p = r_q = 0.85, 0.95, 1.00, 1.05, 1.15$ are assumed. The second Fourier coefficient is set to the fixed value of $\tilde{\lambda}_{pd2} = \tilde{\lambda}_{pc2} = \tilde{\lambda}_{gd2} = \tilde{\lambda}_{gc2} = 0.01$.

The analysis results shown in Fig. 5 indicate that the asymmetric nonlinearity of directional rotation radii only affects the dynamic displacement response in the double-sided tooth impact range. The peak frequency of the primary resonance increases as the ratio of the directional rotation radius mean value of coast side over the drive side one increases as shown in the enlarged plot Fig. 5(b).

4.2.3 Effect of mesh stiffness variation

In this analysis, similar to the directional rotation radii study discussed above, the mesh stiffness is assumed symmetric with $r_k = 1$, in order to examine the effect of mesh stiffness variation. Five different groups of second and third Fourier coefficients of the mesh stiffness values given by $(\tilde{k}_{d2} = \tilde{k}_{c2}, \tilde{k}_{d3} = \tilde{k}_{c3}) = (-0.0405, 0.0294), (-0.081, 0.0588), (-0.162, 0.1176), (-0.243, 0.1764), (-0.324, 0.2352)$ are specified.

As shown in Fig. 6, when the second and third Fourier coefficients of the mesh stiffness increase, the peak values of the super-harmonic resonances are amplified and both the resonance frequency and peak values of the primary resonance are amplified as well. This trend is similar to the directional rotation radius results.

4.2.4 Effect of mesh stiffness asymmetric nonlinearity

Five different ratio values given by $r_k = 0.25, 0.50, 1.00, 2.00, 4.00$ of mesh stiffness mean value of coast side over the drive side one are selected to check their

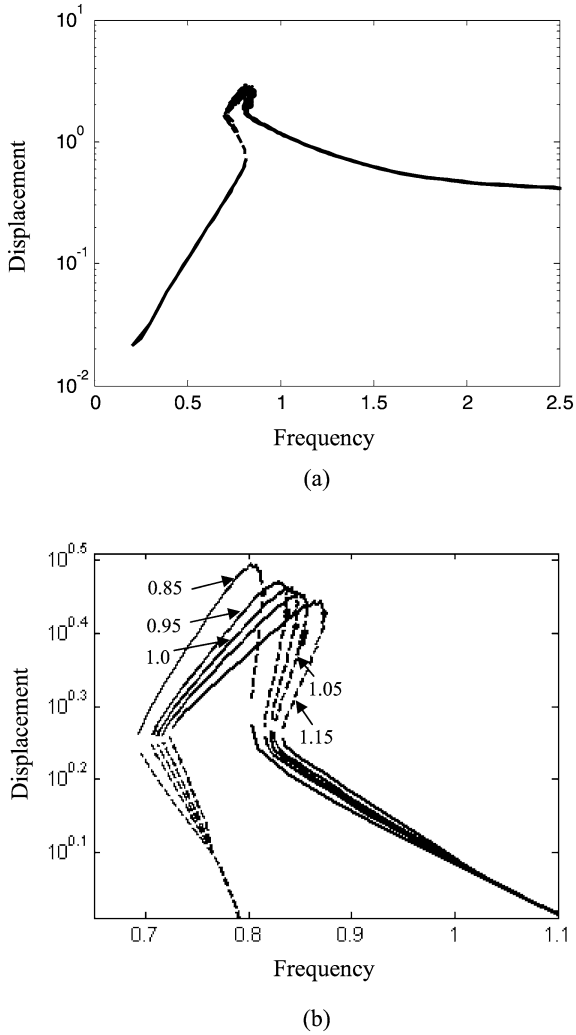

Fig. 5 Effect of directional rotation radii asymmetric nonlinearity on the dynamic response: (**a**) RMS of the dynamic displacement, (**b**) primary resonance of the dynamic displacement. ——— Stable steady-state solution by multi-term HBM; – – – · Unstable steady-state solution by multi-term HBM

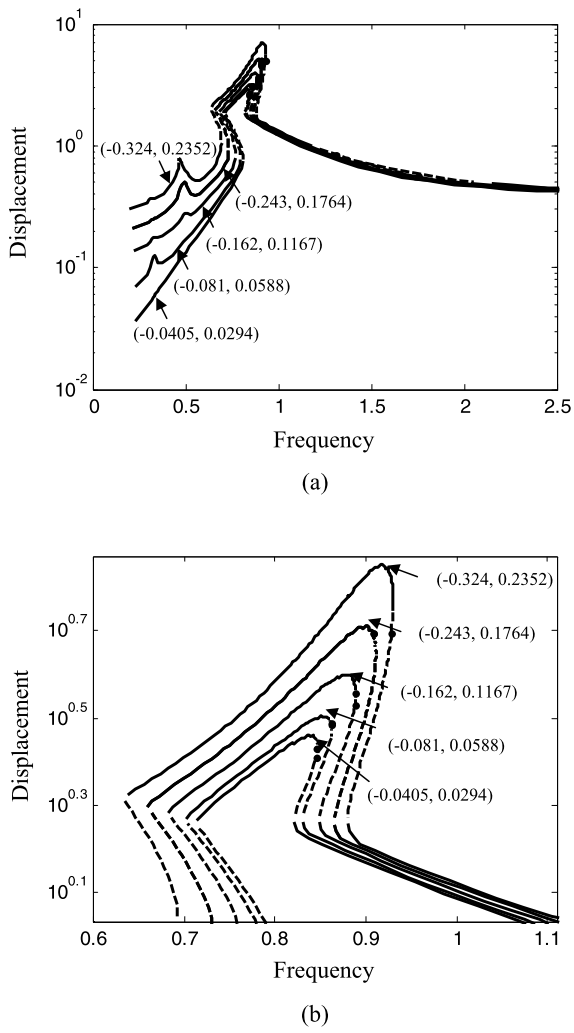

Fig. 6 Effect of the mesh stiffness variation on the dynamic response: (**a**) RMS of the dynamic displacement, (**b**) primary resonance of the dynamic displacement. ——— Stable steady-state solution by multi-term HBM; – – – · Unstable steady-state solution by multi-term HBM

effects on the dynamic displacement responses. The second and third Fourier coefficients of the mesh stiffness are set to the fixed set of $(\tilde{k}_{d2} = \tilde{k}_{c2}, \tilde{k}_{d3} = \tilde{k}_{c3}) = (-0.0405, 0.0294)$.

In Fig. 7, the mesh stiffness asymmetry nonlinearity can be seen to only affect the dynamic displacement response in the double side impact range. This is again similar to the directional rotation radius study. The frequency of the primary resonance increases as the ratio of the mesh stiffness mean value of coast side over the drive side one increases. The effect appears like a hardening spring, as seen in the enlarged plot Fig. 7(b). When $r_k = 0.25$ and $r_k = 0.5$, all the double-sided tooth impact steady-state solutions remain stable, which means that the mesh stiffness asymmetric nonlinearity seems to affect the stability of the steady-state solution of the double-sided tooth impact. This is because that double-sided impact behaves similarly to a hardening spring, as seen from earlier results. As the ratio of mean value of coast side over the drive side one decreases, the effect of hardening spring becomes weaker, and the solution trajectory veers lesser to the right. As a result, for the case $r_k = 0.25$ and $r_k = 0.5$, when gear pair undergoes the transition from single-

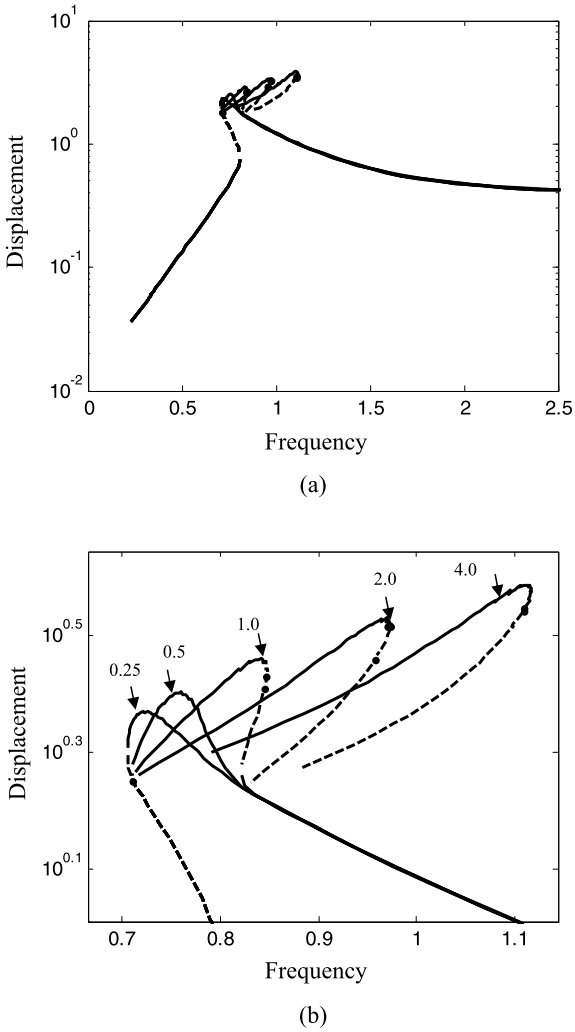

Fig. 7 Effect of the mesh stiffness asymmetry nonlinearity on the dynamic response: (**a**) RMS of the dynamic displacement, (**b**) primary resonance of the dynamic displacement. ——— Stable steady-state solution by multi-term HBM; – – – · Unstable steady-state solution by multi-term HBM

sided tooth impact to double-sided tooth impact with the frequency sweeping down, there is no jump phenomenon seen in these cases at all. For the limiting case when the ratio of mean value of coast side and the drive side one equals zero, there is no double-sided tooth impact, and the solution trajectory does not veer to the right.

5 Conclusion

A nonlinear time-varying dynamic model for right-angle gear pair, considering both the backlash and mesh coupling asymmetric nonlinearity, is formulated. The resultant equation of motion is solved for the period-one dynamics using the multi-term harmonic balance method (HBM) coupled with a modified discrete Fourier Transform procedure and numerical continuation method. The accuracy of the HBM solution is demonstrated by comparison to the computationally more intensive direct numerical integration solutions. The Floquet theory is applied to determine the stability of the steady-state harmonic balance solutions.

A light load case using the example of a right-angle hypoid gear set is chosen for the parametric studies. The effects of the variation of mesh stiffness and directional rotation radii and their asymmetric nonlinearity on the dynamic displacement are analyzed. The increase in the variation of directional rotation radii and mesh stiffness can be seen to amplify the magnitude of the super-harmonic responses, and also raise both the magnitude and resonance frequency of the primary resonances. On the other hand, the directional rotation radius and mesh stiffness asymmetric nonlinearity seems to only affect the double-sided tooth impact response. The increase of the ratio of directional rotation radius mean value of coast side over drive side one seems to amplify both the magnitude and resonance frequency of the primary resonance. The increase of the ratio of mesh stiffness mean value of coast side over drive side more substantially amplifies both the magnitude and peak frequency of the primary resonance. Furthermore, the existence of mesh stiffness asymmetry nonlinearity influence the stability of the double-sided tooth impact steady-state solution and the transition between single and double-sided tooth impacts, and thus affect the existence of the jump phenomenon.

References

1. Comparin, R.J., Singh, R.: Non-linear frequency response characteristics of an impact pair. J. Sound Vib. **134**(2), 259–290 (1989)
2. Kahraman, A., Singh, R.: Non-linear dynamics of a spur gear pair. J. Sound Vib. **142**(1), 49–75 (1990)
3. Kahraman, A., Singh, R.: Interactions between time-varying mesh stiffness and clearance non-linearity in a geared system. J. Sound Vib. **146**(1), 136–156 (1991)
4. Blankenship, G.W., Kahraman, A.: Steady state forced response of a mechanical oscillator with combined parametric excitation and clearance type non-linearity. J. Sound Vib. **185**(5), 743–765 (1995)

5. Kahraman, A., Blankenship, G.W.: Interaction between commensurate parametric and forcing excitations in a system with clearance. J. Sound Vib. **194**(3), 317–336 (1996)
6. Theodossiades, S., Natsiavas, S.: Non-linear dynamics of gear-pair systems with periodic stiffness and backlash. J. Sound Vib. **229**(2), 287–310 (2000)
7. Ma, Q., Kahraman, A.: Period-one motions of a mechanical oscillator with periodically time-varying, piecewise nonlinear stiffness. J. Sound Vib. **284**, 893–914 (2005)
8. Ma, Q., Kahraman, A.: Subharmonic resonances of a mechanical oscillator with periodically time-varying, piecewise non-linear stiffness. J. Sound Vib. **294**, 624–636 (2006)
9. Al-shyyab, A., Kahraman, A.: Non-linear dynamic analysis of a multi-mesh gear train using multi-term harmonic balance method: period-one motions. J. Sound Vib. **284**, 151–172 (2005)
10. Al-shyyab, A., Kahraman, A.: Non-linear dynamic analysis of a multi-mesh gear train using multi-term harmonic balance method: sub-harmonic motions. J. Sound Vib. **279**, 417–451 (2005)
11. Kahraman, A., Singh, R.: Non-linear dynamics of a geared rotor-bearing system with multiple clearances. J. Sound Vib. **144**(3), 469–506 (1991)
12. Al-shyyab, A., Kahraman, A.: A non-linear dynamic model for planetary gear sets. Proc. Inst. Mech. Eng., Part K: J. Multi-Body Dyn. **221**(4), 567–576 (2007)
13. Maatar, M., Velex, P.: An analytical expression for time-varying contact length in perfect cylindrical gears: some possible applications in gear dynamics. J. Mech. Des. **118**, 586–589 (1996)
14. Ajim, M., Velex, P.: A model for simulating the quasi-static and dynamic behavior of solid wide-faced spur and helical gears. Mech. Mach. Theory **40**, 173–190 (2005)
15. Ozguven, H.N., Houser, D.R.: Mathematical models used in gear dynamics—a review. J. Sound Vib. **121**(3), 383–411 (1988)
16. Kiyono, S., Fujii, Y., Suzuki, Y.: Analysis of vibration of bevel gears. Bull. JSME **14**, 441–446 (1981)
17. Abe, E., Hagiwara, H.: Advanced method for reduction in axle gear noise, Gear Design, Manufacturing and Inspection Manual (Society of Automotive Engineerings, Warrendale, PA), 223–236 (1990)
18. Lim, T.C., Cheng, Y.: A theoretical study of the effect of pinion offset on the dynamics of hypoid geared rotor system. J. Mech. Des. **121**, 594–601 (1999)
19. Cheng, Y., Lim, T.C.: Vibration analysis of hypoid transmissions applying an exact geometry-based gear mesh theory. J. Sound Vib. **240**, 519–543 (2001)
20. Cheng, Y., Lim, T.C.: Dynamic analysis of high speed hypoid gears with emphasis on the automotive axle noise problem. In: Proceeding of the ASME Power Transmission and Gearing conference, DETC98/PTG-5784, Atlanta, GA (1998)
21. Cheng, Y., Lim, T.C.: Dynamics of hypoid gears transmission with time-varying mesh. In: Proceeding of the ASME Power Transmission and Gearing conference, DETC2000/PTG-14432, Baltimore, MD (2000)
22. Cheng, Y.: Dynamics of high-speed hypoid and bevel geared rotor systems. Ph.D. dissertation, Ohio State University (2000)
23. Jiang, X.: Non-linear torsional dynamic analysis of hypoid gear pairs. M.S. thesis, University of Alabama (2002)
24. Wang, H.: Gear mesh characteristics and dynamics of hypoid gear rotor system. Ph.D. dissertation, University of Alabama (2002)
25. Wang, J., Lim, T.C., Li, M.: Dynamics of a hypoid gear pair considering the effects of time-varying mesh parameters and backlash nonlinearity. J. Sound Vib. **308**, 302–329 (2007)
26. Wang, J., Lim, T.C.: Effect of tooth mesh stiffness asymmetric nonlinearity for drive and coast sides on hypoid gear dynamics. J. Sound Vib. **319**, 885–903 (2009)
27. Kim, T.C., Rook, T.E., Singh, R.: Super- and sub-harmonic response calculations for a torsional system with clearance nonlinearity using harmonic balance method. J. Sound Vib. **281**, 965–993 (2005)
28. Allgower, E.L., Georg, K.: Numerical Continuation Methods: An Introduction. Springer, New York (1990)
29. Nayfeh, A.H., Mook, D.T.: Nonlinear Oscillations. Wiley, New York (1979)